

# Charge state equilibration of nitrogen-vacancy center ensembles in diamond: The role of electron tunneling

Audrius Alkauskas,<sup>1,\*</sup> Chris G. Van de Walle,<sup>2</sup> Lukas Razinkovas,<sup>1,†</sup> and Ronald Ulbricht<sup>3,‡</sup>

<sup>1</sup>*Department of Fundamental Research, Center for Physical Sciences and Technology (FTMC), Vilnius LT-10257, Lithuania*

<sup>2</sup>*Materials Department, University of California, Santa Barbara, California 93106-5050, USA*

<sup>3</sup>*Max Planck Institute for Polymer Research, Ackermannweg 10, 55128 Mainz, Germany*

The charge state stability of nitrogen-vacancy (NV) centers critically affects their application as quantum sensors and qubits. Understanding charge state conversion and equilibration is critical not only for NV centers in diamond but also for defects and impurities in wide-bandgap materials in general. The mechanisms by which these centers change charge state upon optical or electronic excitation without the presence of mobile carriers remain unclear, potentially affecting the performance of applications ranging from phosphors to power electronics. Here, we elucidate this issue for the case of photoionization of NV center ensembles. Using pump-probe spectroscopy, we ionize negatively charged NV centers and monitor the recovery of  $NV^-$  on timescales of up to several seconds. We find that the recovery rate depends strongly on the concentration of surrounding nitrogen donors. Remarkably, the equilibration dynamics exhibit no discernible dependence on temperature, ruling out thermally activated processes. The multiphonon-assisted electron tunneling model, supported by density-functional calculations, explains the measurements and identifies tunneling as the equilibration mechanism.

The nitrogen-vacancy (NV) center in diamond [1] has become a versatile platform for testing and implementing quantum technologies in sensing, communication, and computing [2–6]. The negatively charged state ( $NV^-$ ) is pivotal for these applications because it offers the required optical and spin properties. Interactions with nearby deep-level dopants affect the equilibrium charge state of the NV center [7]. To establish the negative charge state, NV typically captures an electron from a neighboring single-substitutional nitrogen (N) defect, forming an  $NV^-N^+$  pair [8]. Such charge transfer between deep-level defects cannot be explained by the Shockley-Read-Hall model [9, 10], which depends on thermal excitation and carrier capture. For deep defects with high ionization energies, this mechanism is ineffective, suggesting that electron tunneling is responsible for the charge transfer [8]. Electron tunneling from the excited state of  $NV^-$  to nearby  $N^+$  defects has also been proposed as a mechanism for quenching  $NV^-$  photoluminescence (PL) [11, 12]. Related studies of direct inter-defect charge transfer in silicon [13] and tunneling through deep levels in quantum-dot heterostructures [14] highlight that tunneling between localized states can be highly efficient. Despite suggestions, there is a lack of experimental or theoretical evaluations. Understanding these mechanisms is essential for applications beyond the NV center, where optical or electronic excitation alters the charge state of deep defects or impurities in wide-bandgap semiconductors or insulators, such as phosphors, scintillators, or devices with (semi-)insulating layers.

In this Letter, we investigate the charge equilibration dynamics of an ensemble of NV centers following photoionization, which converts  $NV^-$  centers to the neutrally charged  $NV^0$  state. Our transient spectroscopy

results reveal that the recovery dynamics back to  $NV^-$  are governed by the concentration of N centers with no discernible dependence on temperature. We propose that the charge equilibration occurs via phonon-assisted electron tunneling between  $N^0$  and  $NV^0$ , facilitated by significant lattice relaxation of the N center. This hypothesis is supported by density functional theory (DFT) calculations of the electron-phonon interaction. We also provide a microscopic empirical model that replicates the observed dynamics and explains the lack of temperature dependence. Our approach should be applicable to other materials containing ensembles of deep-level defects, where electron tunneling serves as the mechanism for charge migration and equilibration.

Optical excitation can photoionize  $NV^-$  by promoting an electron to the conduction band (CB), thereby converting  $NV^-$  to  $NV^0$  [15–18]. The threshold for direct ionization is estimated to lie between 2.6 and 2.74 eV, based on both experimental [17, 19] and theoretical [18–20] studies. Time-resolved THz spectroscopy shows that electrons photoexcited from N to the CB recombine back to N within tens of picoseconds [21, 22], indicating a strong recombination pathway. A similar recombination with N is likely to follow photoionization of NV. The ionization threshold of N from the neutral to the positively charged state is approximately 1.7 eV [7, 23]. The resulting model of the tunneling transition that equilibrates the charge after photoionization is depicted in Fig. 1(a), illustrating the charge state transition (CST) levels: (0/–) for the NV center and (+/0) for the N defect. The tunneling of an electron from  $N^0$  to  $NV^0$  is an exothermic process that releases approximately 1 eV of energy.

To establish a theoretical foundation for the tunneling process, we consider the multiphonon emission mecha-

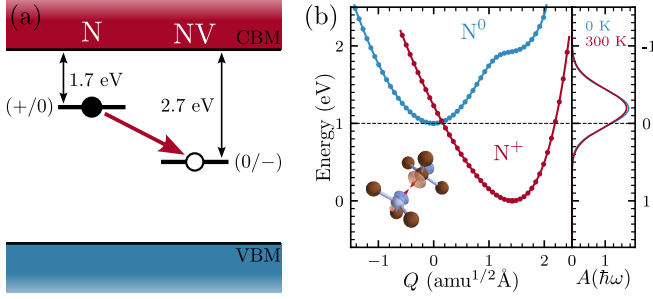


FIG. 1. Phonon-assisted electron tunneling from  $N^0$  to  $NV^0$ . (a) Exothermic charge transfer: the ionization threshold for  $N^0$  is 1.7 eV, and the energy released when the electron is captured by  $NV^0$  is about 2.7 eV. (b) Left: first-principles configuration coordinate (CC) potential energy surfaces of the N center. Inset: atomic structure of  $N0$  with antibonding orbital isosurfaces in neutral state; arrows show atomic motion along the positive CC  $Q$  direction. Right: Optical spectral functions for the tunneling process at  $T = 0$  K and 300 K, where the value at  $E = 0$  corresponds to the vibrational factor  $A(\Delta E; 0)$  in Eq. (1).

nism, which involves an energy-conserving transition followed by rapid vibrational relaxation to thermal equilibrium; this relaxation typically occurs on picosecond timescales [24, 25]. We employ a simplified microscopic model with three degrees of freedom: one for the electron and two for the vibrational motion associated with the NV center and the N donor, respectively. The charge tunneling rate between two spatially separated states in the coupled NV–N system is described by Fermi’s golden rule:

$$\Gamma = \frac{2\pi}{\hbar} W_{fi}^2 A(\Delta E; 0), \quad (1)$$

where  $W_{fi}$  is the hopping matrix element representing the electronic charge transfer between the initial ( $i$ ) and final ( $f$ ) electronic states. The vibrational factor  $A(\Delta E, 0)$  reflects the probability that the energy difference between the initial and final electronic states is entirely transferred to the vibrational system, allowing a non-radiative transition. This factor corresponds to the value of the normalized spectral function  $A(\Delta E; \hbar\omega)$  at  $\hbar\omega = 0$ , which describes the spectral density of phonon-assisted radiative transitions [26, 27]. In our model, this spectral function takes the form:

$$A(\Delta E, \hbar\omega) = \sum_{mlnk} w_m(T) w_l(T) |\langle \chi_{fn}^N | \chi_{im}^N \rangle \langle \chi_{fk}^{NV} | \chi_{il}^{NV} \rangle|^2 \times \delta(\Delta E + \varepsilon_{i;ml} - \varepsilon_{f;nk} - \hbar\omega), \quad (2)$$

where  $\varepsilon_{i;ml}$  represents the vibrational energy of the system in the  $i$  electronic state, with N and NV having  $m$  and  $l$  excited phonons, respectively. The factors  $w_l(T)$  are Boltzmann weights that account for the temperature-dependent occupation of vibrational states.

The vibrational overlap integrals,  $\langle \chi_{fn} | \chi_{il} \rangle$ , quantify the coupling between vibrational states in the initial and final electronic manifolds. This electron-phonon interaction is commonly characterized by the Huang–Rhys (HR) factor  $S$  [28], which represents the average number of phonons excited during an electronic transition. For the NV center, the HR factor for the  $(0/-)$  charge-state transition is  $S \approx 1.3$  [18], indicating a low probability of exciting more than two phonons. In contrast, the N defect exhibits much stronger electron-phonon coupling, with  $S \gg 1$  [29], making it the dominant contributor to the lineshape function. This pronounced coupling arises from its structural configuration:  $N^0$  lacks a covalent bond with one adjacent carbon, forming an antibonding orbital in the region of the missing bond [see inset of Fig. 1(b)]. In its neutral state, this orbital is occupied, and the removal of the electron restores the covalent bond, leading to significant lattice relaxation. Given the distinct electron-phonon interactions, we assume  $\langle \chi_{fn}^{NV} | \chi_{im}^{NV} \rangle = \delta_{nm}$ , meaning the N defect solely determines the vibrational factor in Eq. (2). This simplifies the model’s functional form to the well-known 1D problem of carrier capture at point defects [26, 30].

We investigate the electron-phonon interaction of the N defect using DFT calculations within the one-dimensional configurational coordinate (CC) approximation [27]. The calculations were performed using the VASP code [31] with the  $r^2$ SCAN density functional [32], which has proven effective in describing electron–phonon interactions in various deep-level defects [33–36]. Computational details are available in Sec. S1 of the Supplemental Material (SM) [37].

The right side of Fig. 1(b) shows the CC potential energy surfaces for electron tunneling from the neutral N defect to the neutral NV center, with a vertical offset of  $\Delta E = 1$  eV. Both surfaces exhibit strong anharmonicity due to pronounced electron–phonon interaction. To accurately compute the spectral function (2), we numerically solved the one-dimensional nuclear Schrödinger equation. The left side of Fig. 1(b) shows spectral functions  $A(\Delta E; \hbar\omega)$  calculated at  $T = 0$  and 300 K. The approximate Huang–Rhys (HR) factor, estimated as the average number of emitted phonons, is  $S \approx 14$ . The vibrational factor  $A(\Delta E; 0)$  corresponds to the no-photon-emission condition, and is represented by the horizontal dashed line. Notably, for  $\Delta E = 1$  eV, the factor is near peak efficiency, indicating an effective channel for non-radiative tunneling. The calculated vibrational factor values are  $A(1, 0) = 1.19 \text{ eV}^{-1}$  at  $T = 0$  and  $1.16 \text{ eV}^{-1}$  at 300 K, indicating minimal temperature dependence.

For completeness, we also examined an alternative pathway where the  $NV^-$  center transitions to the metastable singlet  $^1E$  state, located  $\sim 0.4$  eV above the ground  $^3A_2$  level [38]. However, the vibrational factors for this transition are about 50 times smaller [ $A(0.6, 0) = 0.05 \text{ eV}^{-1}$  at  $T = 0$  and  $0.07 \text{ eV}^{-1}$  at 300 K], making this

pathway much less significant compared to the transition to the ground state.

For a qualitative estimate of the electronic transition matrix element  $W_{fi}$  and its dependence on distance, we employ the effective-mass approximation and the zero-range potential (ZRP) model [39–41] to approximate the short-range potential of deep-level defects. In this model, the wavefunction is expressed as:

$$\psi_i(r) = \sqrt{\frac{\alpha_i}{2\pi}} \frac{e^{-\alpha_i r}}{r}, \quad (3)$$

where  $r$  is the radial distance from the defect center. Within the effective-mass approximation, the parameter  $\alpha_i = \sqrt{2mE_i}/\hbar$  is determined by the ionization energy  $E_i$ . In the ZRP model, the short-range potential is replaced by a boundary condition requiring that the logarithmic derivative of the radial part  $r\psi_i$  equals  $-\alpha_i$ .

The electron transfer matrix element, analogous to the hopping term in a tight-binding model, can be expressed as  $W_{fi} = E_{NV} \langle \psi_{NV} | \psi_N \rangle + \langle \psi_{NV} | V_{NV} | \psi_N \rangle$  [14]. Here,  $E_{NV}$  is the negative binding energy of the NV center electron,  $\psi_{NV}$  and  $\psi_N$  are the localized wavefunctions of the isolated NV and N defects, and  $V_{NV}$  is the potential of the NV center. Within the ZRP model, the matrix element is derived as follows (see Sec.S2 of the SM [37] for details):

$$W_{fi} = \frac{\hbar^2}{mr} \frac{\sqrt{\alpha_1 \alpha_2}}{(\alpha_1^2 - \alpha_2^2)} (\alpha_2^2 e^{-\alpha_1 r} - \alpha_1^2 e^{-\alpha_2 r}), \quad (4)$$

where  $r$  is the separation between the centers.

To model the population dynamics of ionized NV centers, we assume that the electron tunnels from the nearest  $N^0$  defect. This assumption is justified by the experimental protocol, which involves repeated intense optical pulses that ionize the  $NV^-$  centers and redistribute the local charge. As a result, the probability of finding a nearby positively charged nitrogen ( $N^+$ ) immediately after excitation is significantly reduced. We therefore assume that nearly all substitutional nitrogen remains in the neutral charge state. The radial probability distribution of finding the nearest neighbor in the radial shell between  $r$  and  $r + dr$  is given by [42]:

$$w(r) = 4\pi r^2 n e^{-\frac{4}{3}\pi n r^3}.$$

where  $n$  is the overall density of nitrogen defects. The function  $w(r)$  peaks at a distance of  $(2\pi n)^{-1/3}$ , corresponding to 44.9, 20.9, and 17.1 Å for nitrogen concentrations of 10, 100, and 180 ppm, respectively.

Using the above distribution of nearest N donors, the temporal dependence of the relative concentration of neutral NV centers,  $p(t) = [NV^0](t)/[NV^0](0)$ , due to tunneling from N defects, becomes:

$$p(T, t) = \int_0^\infty w(r) e^{-\Gamma(r; T) t} dr. \quad (5)$$

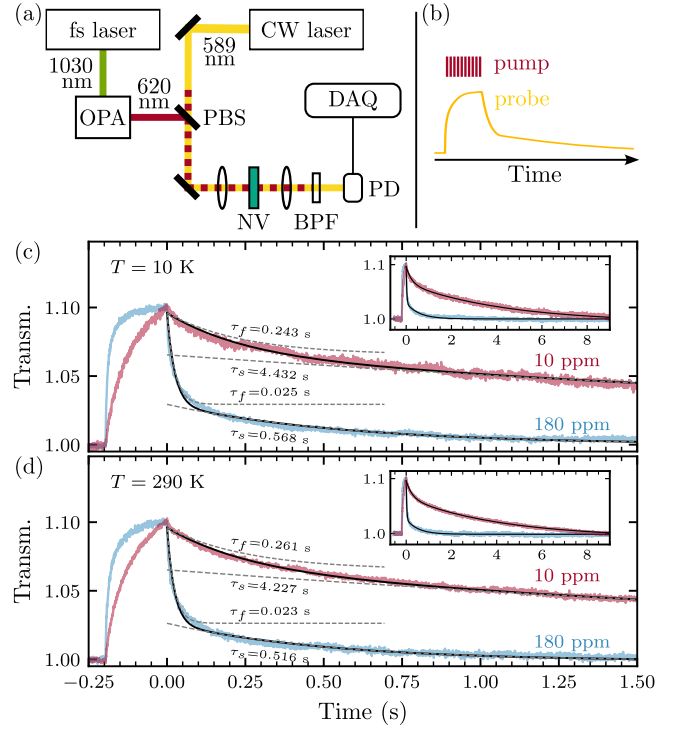


FIG. 2. (a) Schematic of the measurement setup. Abbreviations: OPA – optical parametric amplifier, PBS – polarizing beam splitter, BPF – bandpass filter, PD – photodiode, DAQ – Data acquisition card; (b) Excitation scheme illustrating pump and probe dynamics; Normalized probe transmission dynamics for both samples at temperatures of (c) 10 K and (d) 290 K, with bi-exponential fits to the data. The inset plots display graphs for a 10 s time window.

Having established a theoretical framework for modeling charge equilibration dynamics via electron tunneling, we now turn to experimental verification. We employ a pump–probe spectroscopy setup using two diamond substrates having low (10 ppm) and high (180 ppm) N concentrations. A pulsed pump laser ionizes the NV ensemble, while a continuous-wave (CW) laser monitors the time-resolved transmission through the sample [43]. The setup is illustrated in Fig. 2(a), with additional details provided in Sec. S4 of the SM [37].

In brief, pump pulses with a duration of approximately 150 fs at a wavelength of 620 nm are emitted at a 10 kHz repetition rate. For the considered timescales, the pulsed excitation can be treated as a continuous excitation. The chosen wavelength selectively excites and, via resonant two-photon absorption [18], ionizes  $NV^-$  without exciting  $NV^0$ . The CW probe laser emits at a wavelength of 589 nm, again selectively addressing  $NV^-$  without exciting  $NV^0$ . The time-resolved measurement of the transmitted probe beam enables monitoring of the transient bleaching of the  $NV^-$  absorption. Figures 2(c) and (d) show the normalized probe transmission dynamics for both samples at 10 and 290 K, respectively, with the

pre-pump signal set to unity and the maximum set to 1.1. The pump laser excites the sample for 200 ms, steadily building a non-equilibrium concentration of  $\text{NV}^0$  centers, as evidenced by an increase in the probe transmission, i.e., bleaching of  $\text{NV}^-$  absorption. After switching off the pump, the system relaxes towards equilibrium for up to 10 seconds while the probe laser monitors the process. This cycle is repeated several times, and the recorded transient transmission data are averaged.

The relaxation dynamics can be approximately described by a bi-exponential model, as indicated by the fits shown in Figs. 2(c) and (d), where the corresponding characteristic time constants are displayed. Notably, the dynamics remain nearly identical at both cryogenic and room temperatures. A more quantitative analysis is provided in Sec. S4 of the SM [37], where the extracted time constants are plotted as a function of temperature for both samples, confirming the temperature independence predicted by our model.

To relate the theoretical model to the experimental conditions, we now consider the population buildup during the pumping stage. Applying ionizing excitation results in the accumulation of a population of  $\text{NV}^0$  centers with longer equilibration times, while effectively filtering out contributions with tunneling rates higher than the average ionization rate. Accordingly, Eq. (5) is adjusted as:

$$p_{\text{eff}}(T, t) = \int_0^\infty f(\tau[r; T]) w(r) e^{-\Gamma(r; T)t} dr, \quad (6)$$

where  $f(\tau)$  is a filter function that describes how the population redistributes due to the pumping sequence, and  $\tau = 1/\Gamma(r; T)$  is the tunneling lifetime, which depends on the distance between NV and N centers. The function  $f(\tau)$  can be estimated by treating the pulsed excitation as continuous, replacing the pump sequence with a constant average rate  $G$ . In the weak-excitation limit ( $G \ll \Gamma$ ), the steady-state population after a pump duration  $\Delta t$  takes the form (see Sec. S3 of the SM for details):

$$f(\tau) = G\tau \left(1 - e^{-\Delta t/\tau}\right). \quad (7)$$

The empirical model introduced above relies on two phenomenological parameters,  $\alpha_1$  and  $\alpha_2$ , which describe the spatial extent of the N and NV wavefunctions, respectively. Assuming an effective electron mass of  $m = 0.57 m_e$ , corresponding to the average conduction-band mass in diamond, and using a pump duration of  $\Delta t = 0.2$  s, we simultaneously fit these parameters to the experimental decay curves at  $T = 10$  K measured for both nitrogen concentrations. To enable direct comparison with the experiment, the simulated and experimental decay curves are normalized such that the pre-pump population is set to unity and the minimum value at  $t = 9$  s is set to 0. Figure 3(a) shows the fitted curve overlaid

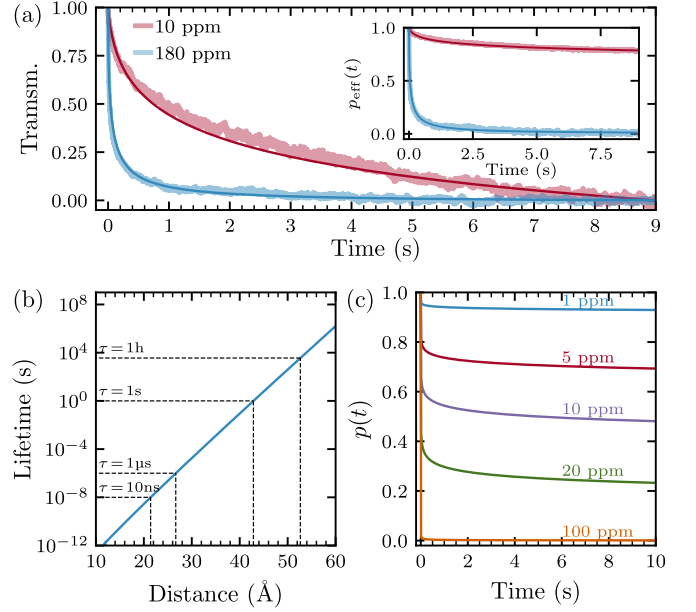


FIG. 3. (a) Simultaneous fit of the empirical tunneling model (thin solid lines) to the experimental decay curves at  $T = 10$  K (thick blurry lines) for 10 ppm and 180 ppm nitrogen concentrations. Both datasets are normalized such that the pre-pump population is one and the value at 9 s is zero. Inset: Same data plotted on an absolute scale, with experimental curves rescaled to match the predicted population difference. (b) Calculated tunneling lifetime  $\tau = 1/\Gamma$  as a function of NV-N separation at  $T = 0$  K. (c) Time evolution of the relative  $\text{NV}^0$  population  $p(t)$  at  $T = 0$  K for different N concentrations (1–100 ppm), following a single-pulse ionization.

on the measured data. The inset presents both simulated and experimental curves on an absolute population scale, with the experimental data rescaled so that the population change over the 9-second interval matches the prediction of the theoretical fit. The model accurately captures the qualitative shape of the probe transmission and reproduces the overall trend observed in both nitrogen concentration samples, highlighting the difference between the two populations. The fitted parameters are  $\alpha_1 = 0.40 \text{ \AA}^{-1}$  and  $\alpha_2 = 0.89 \text{ \AA}^{-1}$ . These values are comparable to those predicted by the phenomenological effective mass expression  $\alpha_i = \sqrt{2mE_i}/\hbar$ , which yields  $0.51 \text{ \AA}^{-1}$  and  $0.64 \text{ \AA}^{-1}$  for the respective ionization energies.

While the extracted parameters provide only a rough estimate, we assume that they capture the core aspects of the tunneling process and use them to determine the associated relaxation lifetimes. Figure 3(b) shows the calculated tunneling lifetime  $\tau = 1/\Gamma$  as a function of NV-N separation at  $T = 0$  K. The lifetime increases rapidly with distance, reflecting the strong exponential sensitivity of the tunneling process. According to our model, tunneling occurs on the nanosecond timescale when N donors lie within 20  $\text{\AA}$  of an NV center but reaches hours

if the separation is above 50 Å. Such rapid decay at NV–N separations up to 20 Å qualitatively aligns with the estimate in Ref. [8], which suggests that  $NV^-$  centers appear dark if a positively charged N defect is within 12 Å, due to electron tunneling from the excited state of  $NV^-$  to a nearby  $N^+$  center. Although the underlying process differs, the energy released by tunneling from  $NV^-$  to  $N^+$  is also on the order of 1 eV, and the electron–phonon interaction strength is expected to be of similar magnitude due to the involvement of a charge state change of the N defect.

Figure 3(c) displays the theoretical prediction for how the relative fraction of  $NV^0$  centers evolves over time at  $T = 0$  K for N donor concentrations of 1, 5, 10, 20, and 100 ppm, assuming a single short-pulse ionization [Eq. (5)]. On a linear scale, the decay dynamics exhibit two distinct regimes: an initial rapid decrease in  $p(t)$ , followed by a much slower decay, a characteristic behavior also observed in our experimental measurements with a finite pre-pump time. For the nitrogen concentrations considered here, the slow-decay regime can extend over several seconds. For example, at 10 ppm, the model predicts that  $p(t)$  remains above 0.48 even after ten seconds. At higher nitrogen concentrations, charge equilibration happens much faster: at 20 ppm, the population drops to 0.23 after 10 s, while at 100 ppm, it falls below 1% ( $p(t) = 0.001$ ) in less than 100 ms. At lower nitrogen concentrations, charge equilibration slows down significantly. For the 1 ppm case, our model predicts that only 11% of the population recovers after one hour ( $p(t) = 0.89$ ).

Our combined experimental and theoretical analysis identifies electron tunneling between N donors and NV centers as the primary mechanism governing charge-state equilibration in ensembles. The results provide a quantitative basis for predicting NV charge stability and establish an experimental protocol for directly probing defect–defect charge transfer. Future research could explore how surface-induced band bending alters defect energetics and tunneling rates, particularly in sensing applications where NV centers are deliberately positioned near the surface. Achieving a comprehensive understanding of NV charge stability will also involve analyzing how other deep dopants in diamond influence these dynamics and how charge transfer among dopants (such as the movement of positive charge among nitrogen centers) alters the local charge environment. Our framework should also be applicable to other deep-level defects in wide-bandgap materials, especially in regimes where carrier interaction with the bands is suppressed and tunneling governs charge migration.

*Acknowledgments*—We thank Neil Manson for many helpful discussions and Vytautas Karpus for introducing us to the zero-range potential model. C. G. VdW. thanks C. Vishwakarma and J. K. Nangoi for useful discussions. R.U. acknowledges support from the Max Planck Society. A.A. and L.R. were supported by the QuantERA grant

SensExtreme, funded by the Lithuanian Research Council (Grant No. S-QUANTERA-22-1). Computational resources were provided by the supercomputer GALAX at the Center for Physical Sciences and Technology, Lithuania, and by the High Performance Computing Center “HPC Saulėtekis” at the Faculty of Physics, Vilnius University. C. G. VdW. was supported by the U.S. Department of Energy, Office of Science, Co-design Center for Quantum Advantage (C2QA) under contract number DE-SC0012704.

*Data availability*—The data that support the findings of this study are available from the corresponding authors upon reasonable request.

---

\* Deceased

† lukas.razinkovas@ftmc.lt

‡ ulbricht@mpip-mainz.mpg.de

- [1] M. W. Doherty, N. B. Manson, P. Delaney, F. Jelezko, J. Wrachtrup, and L. C. Hollenberg, The nitrogen-vacancy colour centre in diamond, *Physics Reports* **528**, 1 (2013).
- [2] R. Schirhagl, K. Chang, M. Loretz, and C. L. Degen, Nitrogen-Vacancy Centers in Diamond: Nanoscale Sensors for Physics and Biology, *Annu. Rev. Phys. Chem.* **65**, 83 (2014).
- [3] B. Hensen, H. Bernien, A. E. Dréau, A. Reiserer, N. Kalb, M. S. Blok, J. Ruitenbergh, R. F. L. Vermeulen, R. N. Schouten, C. Abellán, W. Amaya, V. Pruneri, M. W. Mitchell, M. Markham, D. J. Twitchen, D. Elkouss, S. Wehner, T. H. Taminiau, and R. Hanson, Loophole-free Bell inequality violation using electron spins separated by 1.3 kilometres, *Nature* **526**, 682 (2015).
- [4] D. D. Awschalom, R. Hanson, J. Wrachtrup, and B. B. Zhou, Quantum technologies with optically interfaced solid-state spins, *Nature Photon* **12**, 516 (2018).
- [5] C. E. Bradley, J. Randall, M. H. Aboei, R. C. Berrevoets, M. J. Degen, M. A. Bakker, M. Markham, D. J. Twitchen, and T. H. Taminiau, A Ten-Qubit Solid-State Spin Register with Quantum Memory up to One Minute, *Phys. Rev. X* **9**, 031045 (2019).
- [6] S. Pezzagna and J. Meijer, Quantum computer based on color centers in diamond, *Appl. Phys. Rev.* **8**, 011308 (2021).
- [7] A. T. Collins, The Fermi level in diamond, *J. Phys.: Condens. Matter* **14**, 3743 (2002).
- [8] N. B. Manson, M. Hedges, M. S. J. Barson, R. Ahlefeldt, M. W. Doherty, H. Abe, T. Ohshima, and M. J. Sellars,  $NV^-$ – $N^+$  pair centre in 1b diamond, *New J. Phys.* **20**, 113037 (2018).
- [9] W. Shockley and W. T. Read, Statistics of the Recombinations of Holes and Electrons, *Phys. Rev.* **87**, 835 (1952).
- [10] R. N. Hall, Electron-Hole Recombination in Germanium, *Phys. Rev.* **87**, 387 (1952).
- [11] M. T. Luu, A. Tayefeh Younesi, and R. Ulbricht, Nitrogen-vacancy centers in diamond: Discovery of additional electronic states, *Materials for Quantum Technology* **4**, 035201 (2024).
- [12] M. Capelli, L. Lindner, T. Luo, J. Jeske, H. Abe, S. On-

- oda, T. Ohshima, B. Johnson, D. A. Simpson, A. Stacey, P. Reineck, B. C. Gibson, and A. D. Greentree, Proximal nitrogen reduces the fluorescence quantum yield of nitrogen-vacancy centres in diamond, *New Journal of Physics* **24**, 033053 (2022).
- [13] A. M. Frens, M. T. Bennebroek, A. Zakrzewski, J. Schmidt, W. M. Chen, E. Janzén, J. L. Lindström, and B. Monemar, Observation of rapid direct charge transfer between deep defects in silicon, *Phys. Rev. Lett.* **72**, 2939 (1994).
- [14] P. C. Sercel, Multiphonon-assisted tunneling through deep levels: A rapid energy-relaxation mechanism in non-ideal quantum-dot heterostructures, *Phys. Rev. B* **51**, 14532 (1995).
- [15] K. Beha, A. Batalov, N. B. Manson, R. Bratschitsch, and A. Leitenstorfer, Optimum Photoluminescence Excitation and Recharging Cycle of Single Nitrogen-Vacancy Centers in Ultrapure Diamond, *Phys. Rev. Lett.* **109**, 097404 (2012).
- [16] P. Siyushev, H. Pinto, M. Vörös, A. Gali, F. Jelezko, and J. Wrachtrup, Optically Controlled Switching of the Charge State of a Single Nitrogen-Vacancy Center in Diamond at Cryogenic Temperatures, *Phys. Rev. Lett.* **110**, 167402 (2013).
- [17] N. Aslam, G. Waldherr, P. Neumann, F. Jelezko, and J. Wrachtrup, Photo-induced ionization dynamics of the nitrogen vacancy defect in diamond investigated by single-shot charge state detection, *New J. Phys.* **15**, 013064 (2013).
- [18] L. Razinkovas, M. Maciaszek, F. Reinhard, M. W. Doherty, and A. Alkauskas, Photoionization of negatively charged NV centers in diamond: Theory and *ab initio* calculations, *Phys. Rev. B* **104**, 235301 (2021).
- [19] E. Bourgeois, E. Londero, K. Buczak, J. Hruby, M. Gulka, Y. Balasubramaniam, G. Wachter, J. Stursa, K. Dobes, F. Aumayr, M. Trupke, A. Gali, and M. Nesládek, Enhanced photoelectric detection of NV magnetic resonances in diamond under dual-beam excitation, *Phys. Rev. B* **95**, 041402 (2017).
- [20] P. Deák, B. Aradi, M. Kaviani, T. Frauenheim, and A. Gali, Formation of NV centers in diamond: A theoretical study based on calculated transitions and migration of nitrogen and vacancy related defects, *Phys. Rev. B* **89**, 075203 (2014).
- [21] R. Ulbricht, E. Hendry, J. Shan, T. F. Heinz, and M. Bonn, Erratum: Carrier dynamics in semiconductors studied with time-resolved terahertz spectroscopy [rev. mod. phys. 83, 543 (2011)], *Rev. Mod. Phys.* **89**, 029901 (2017).
- [22] R. Ulbricht, S. T. Van Der Post, J. P. Goss, P. R. Briddon, R. Jones, R. U. A. Khan, and M. Bonn, Single substitutional nitrogen defects revealed as electron acceptor states in diamond using ultrafast spectroscopy, *Phys. Rev. B* **84**, 165202 (2011).
- [23] M. Nesládek, L. M. Stals, A. Stesmans, K. Iakoubovskij, G. J. Adriaenssens, J. Rosa, and M. Vaněček, Dominant defect levels in diamond thin films: A photocurrent and electron paramagnetic resonance study, *Appl. Phys. Lett.* **72**, 3306 (1998).
- [24] V. May and O. Kühn, *Charge and Energy Transfer Dynamics in Molecular Systems*, fourth edition ed. (Wiley-VCH, Weinheim, Germany, 2023).
- [25] R. Ulbricht, S. Dong, A. Gali, S. Meng, and Z.-H. Loh, Vibrational relaxation dynamics of the nitrogen-vacancy center in diamond, *Phys. Rev. B* **97**, 220302 (2018).
- [26] C. H. Henry and D. V. Lang, Nonradiative capture and recombination by multiphonon emission in GaAs and GaP, *Phys. Rev. B* **15**, 989 (1977).
- [27] A. Alkauskas, J. L. Lyons, D. Steiauf, and C. G. Van de Walle, First-Principles Calculations of Luminescence Spectrum Line Shapes for Defects in Semiconductors: The Example of GaN and ZnO, *Phys. Rev. Lett.* **109**, 267401 (2012).
- [28] K. Huang and A. Rhys, Theory of light absorption and non-radiative transitions in  $F^-$ -centres, *Proc. R. Soc. Lond. A* **204**, 406 (1950).
- [29] W. J. P. V. Enkevort and E. H. Versteegen, Temperature dependence of optical absorption by the single-substitutional nitrogen donor in diamond, *J. Phys.: Condens. Matter* **4**, 2361 (1992).
- [30] A. Alkauskas, Q. Yan, and C. G. Van de Walle, First-principles theory of nonradiative carrier capture via multiphonon emission, *Physical Review B* **90**, 075202 (2014).
- [31] G. Kresse and J. Furthmüller, Efficient iterative schemes for *ab initio* total-energy calculations using a plane-wave basis set, *Phys. Rev. B* **54**, 11169 (1996).
- [32] J. W. Furness, A. D. Kaplan, J. Ning, J. P. Perdew, and J. Sun, Accurate and Numerically Efficient  $r^2$  SCAN Meta-Generalized Gradient Approximation, *The Journal of Physical Chemistry Letters* **11**, 8208 (2020).
- [33] M. Maciaszek, V. Žalandauskas, R. Silkinis, A. Alkauskas, and L. Razinkovas, The application of the SCAN density functional to color centers in diamond, *J. Chem. Phys.* **159**, 084708 (2023).
- [34] R. Silkinis, M. Maciaszek, V. Žalandauskas, M. E. Bathen, L. Vines, A. Alkauskas, and L. Razinkovas, Optical lineshapes of the c center in silicon from *ab initio* calculations: Interplay of localized modes and bulk phonons, *Phys. Rev. B* **111**, 125136 (2025).
- [35] R. Silkinis, M. Maciaszek, V. Žalandauskas, M. E. Bathen, L. Vines, A. Alkauskas, and L. Razinkovas, Optical lineshapes of the C center in silicon from *ab initio* calculations: Interplay of localized modes and bulk phonons, *Physical Review B* **111**, 125136 (2025).
- [36] V. Žalandauskas, R. Silkinis, L. Vines, L. Razinkovas, and M. E. Bathen, Theory of the divacancy in 4H-SiC: Impact of Jahn-Teller effect on optical properties, *npj Computational Materials* **11**, 155 (2025).
- [37] See supplemental material [url] for [brief description], which includes refs. [...], .
- [38] M. L. Goldman, M. W. Doherty, A. Sipahigil, N. Y. Yao, S. D. Bennett, N. B. Manson, A. Kubanek, and M. D. Lukin, State-selective intersystem crossing in nitrogen-vacancy centers, *Phys. Rev. B* **91**, 165201 (2015).
- [39] H. Bethe and R. Peierls, Quantum theory of the diplon, *Proc. R. Soc. Lond. A* **148**, 146 (1935).
- [40] G. Lucovsky, On the photoionization of deep impurity centers in semiconductors, *Solid State Communications* **3**, 299 (1965).
- [41] Yu. N. Demkov and V. N. Ostrovskii, *Zero-Range Potentials and Their Applications in Atomic Physics* (Springer US, Boston, MA, 1988).
- [42] S. Chandrasekhar, Stochastic problems in physics and astronomy, *Rev. Mod. Phys.* **15**, 1 (1943).
- [43] A. T. Younesi and R. Ulbricht, Broadband transient absorption spectroscopy using an incoherent white-light source as probe, *Opt. Express* **30**, 38896 (2022).
- [44] R. Ulbricht, S. Dong, I.-Y. Chang, B. M. K. Mariserla,



- K. M. Dani, K. Hyeon-Deuk, and Z.-H. Loh, Jahn-Teller-induced femtosecond electronic depolarization dynamics of the nitrogen-vacancy defect in diamond, *Nat Commun* **7**, 13510 (2016).
- [45] W. P. Carbery, C. A. Farfan, R. Ulbricht, and D. B. Turner, The phonon-modulated jahn-teller distortion of the nitrogen vacancy center in diamond, *Nature Communications* **15**, 8646 (2024).
- [46] L. Robledo, H. Bernien, T. v. d. Sar, and R. Hanson, Spin dynamics in the optical cycle of single nitrogen-vacancy centres in diamond, *New Journal of Physics* **13**, 025013 (2011).

## SUPPLEMENTAL MATERIAL

## S1. FIRST-PRINCIPLES MODELING OF ELECTRON-PHONON INTERACTION

We model the electron-phonon interaction of the N defect using a one-dimensional configurational coordinate (CC) approach [27], which is well-suited for systems with strong electron-phonon coupling, as is the case in this study. In this approach, the complex multi-mode vibrational motion is approximated by a single degree of freedom, the configurational coordinate  $Q$ , which parametrizes the ionic displacement between equilibrium geometries of the defect in two charge states. The total displacement between two geometries,  $\Delta Q$ , in mass-weighted coordinates is given by  $\Delta Q^2 = \sum_{\alpha,i} M_\alpha \Delta R_{\alpha,i}^2$ , where the sum runs over all atoms  $\alpha$  and Cartesian directions  $i$ . Here,  $M_\alpha$  is the atomic mass of species  $\alpha$ , and  $\Delta R_{\alpha,i}$  represents the difference in equilibrium positions between the two charge states. The potential energy surfaces for both charge states are then computed along this parametrized configurational coordinate path.

The calculations were performed using spin-polarized density functional theory (DFT) with exchange and correlation described by the  $r^2$ SCAN functional [32]. We employed the projector-augmented wave (PAW) method as implemented in the VASP code [31], using a plane-wave energy cutoff of 600 eV. The defect was modeled in a  $4 \times 4 \times 4$  face-centered cubic (fcc) supercell containing 512 atoms, with the Brillouin zone sampled at a single  $\Gamma$  point. The equilibrium geometries were optimized until the Feynman–Hellmann forces on each atom were below 0.001 eV/Å.

In Fig. S1(a), we present the geometry of the N defect in its neutral charge state. The absence of a covalent bond with one adjacent carbon reduces the symmetry from  $T_d$  to  $C_{3v}$ . Instead of a covalent bond, a singly occupied antibonding orbital is oriented along the  $C_{3v}$  axis, representing the only N-derived state within the diamond band gap. The nitrogen-carbon bond length to the three nearest neighbors is 1.47 Å, while the bond length along the symmetry axis is 2.03 Å, highlighting significant symmetry breaking. Upon ionization to the positively charged state, electron removal restores  $T_d$  symmetry, with all nitrogen-carbon bond lengths equalized at 1.56 Å. This substantial structural relaxation along the symmetry axis of  $N^0$  leads to strong electron–phonon interaction.

Figures S1(b) and (c) present the potential energy surfaces computed along the configurational coordinate. Both surfaces exhibit strong anharmonicity, making the harmonic approximation inadequate for describing electron–phonon interactions. To accurately compute the vibrational overlap integrals entering the normalized spectral function [see also Eq. (2) of the main text]:

$$A(\Delta E, \hbar\omega) = \sum_{mlnk} w_m(T) |\langle \chi_{fn} | \chi_{im} \rangle|^2 \times \delta(\Delta E + \varepsilon_{i;ml} - \varepsilon_{f;nk} - \hbar\omega), \quad (\text{S1.1})$$

we numerically solve for the vibrational states of both potentials. The Numerov integration scheme combined with a shooting method is used to determine the 30 lowest bound states for each surface. The lowest-lying states are visualized in Figs. S1(b) and (c). These computed states form the basis for evaluating the spectral function (S1.1). To achieve a smooth representation of the multi-mode system [as shown on the right side of Fig. 1(b)], the delta functions are replaced with Gaussians of width  $\sigma = 60$  meV.

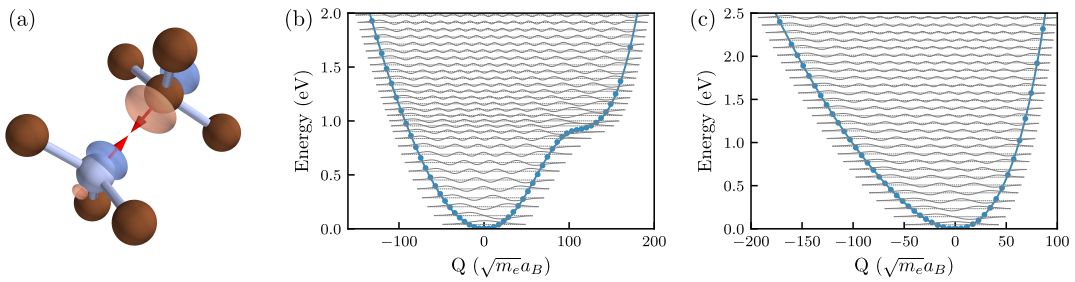


FIG. S1. Ab initio characterization of the electron–phonon interaction in the N defect. (a) Atomic structure of the neutral N center, with isosurfaces showing the antibonding localized orbital occupied in the neutral state; arrows indicate atomic motion along the positive CC  $Q$  direction. (b) and (c) Configurational coordinate (CC) potential energy surfaces for  $N^0$  and  $N^+$ , with dots representing DFT calculations. Numerical solutions of nuclear wavefunctions are shown with baselines shifted according to vibrational state energies.



## S2. ZERO-RANGE POTENTIAL (ZRP) MODEL FOR ELECTRON TUNNELING BETWEEN TWO DEEP-LEVEL DEFECTS

In this section, we develop an analytical expression for the electron tunneling transfer integral between two deep-level defects, focusing on the limit where the binding well width approaches a point-like limit.

### S2.A. Derivation of the Transfer Integral

An electron localized on a deep-level defect site experiences a short-range potential that decays rapidly with distance from the defect. Beyond a certain cutoff distance, we assume that the wave function behaves as that of a free particle. The simplest model to capture this behavior is the zero-range potential (ZRP) model, originally proposed by Bethe and Peierls [39]. In the ZRP model, the wave function beyond the point-like potential is that of a free particle:

$$\psi_i(r) = c_i \frac{e^{-\alpha_i r}}{r}, \quad (\text{S2.2})$$

where  $r = |\mathbf{r} - \mathbf{R}_i|$  denotes the radial distance from the defect located at  $\mathbf{R}_i$ , and  $c_i = \sqrt{\alpha_i/2\pi}$  serves as the normalization constant. The parameter  $\alpha_i = \sqrt{2m(-E_i)}/\hbar$  defines the depth of the potential well, with  $-E_i$  representing the binding (ionization) energy and  $m$  the effective electron mass. Instead of explicitly defining the potential, the ZRP model replaces it with a boundary condition on the logarithmic derivative of the wave function:

$$\frac{1}{r\psi_i} \frac{\partial(r\psi_i)}{\partial r} \bigg|_{r \rightarrow 0} = -\alpha_i.$$

The action of the Hamiltonian describing this potential on its eigenfunction  $\psi_i$  is given by a Green's function equation [41]:

$$\left( -\frac{\hbar^2}{2m} \nabla^2 - E_i \right) \psi_i(\mathbf{r}) = \frac{2\pi\hbar^2}{m} c_i \delta(\mathbf{r} - \mathbf{R}_i). \quad (\text{S2.3})$$

This formulation allows the potential well to be expressed as:

$$V_i = -\frac{2\pi\hbar^2}{m} c_i \delta(\mathbf{r} - \mathbf{R}_i) \frac{1}{\psi_i}. \quad (\text{S2.4})$$

In the basis of two localized wave functions,  $\psi_1$  and  $\psi_2$ , which are the ground-state eigenfunctions of isolated ZRP Hamiltonians with point-like potential wells separated by a distance  $r$ , the zero-order Hamiltonian  $H_0$  describes a system in which each wave function interacts solely with its own local potential, with no influence from the neighboring potential. The Hamiltonian is expressed as:

$$H_0 = \begin{pmatrix} E_1 & 0 \\ 0 & E_2 \end{pmatrix}.$$

When two centers are in proximity, the full Hamiltonian  $H = T + V_1 + V_2$  accounts for the potentials of both ZRP wells,  $V_1$  and  $V_2$ . The matrix elements of the full Hamiltonian, in the basis of the wavefunctions of the isolated system, are given by:

$$\langle \psi_1 | H | \psi_1 \rangle = E_1 + \langle \psi_1 | V_2 | \psi_1 \rangle, \quad (\text{S2.5a})$$

$$\langle \psi_2 | H | \psi_2 \rangle = E_2 + \langle \psi_2 | V_1 | \psi_2 \rangle, \quad (\text{S2.5b})$$

$$\begin{aligned} \langle \psi_1 | H | \psi_2 \rangle &= \langle \psi_1 | T + V_2 | \psi_2 \rangle + \langle \psi_1 | V_1 | \psi_2 \rangle \\ &= -\frac{\alpha_2^2 \hbar^2}{2m} \langle \psi_1 | \psi_2 \rangle - \frac{\sqrt{\alpha_1 \alpha_2} \hbar^2}{rm} e^{-\alpha_2 r}. \end{aligned} \quad (\text{S2.5c})$$

Equation (S2.5c) is derived using the relation  $E_2 = -\alpha_2^2 \hbar^2 / 2m$  and  $\langle \psi_1 | V_1 | \psi_2 \rangle = -(2\pi\hbar^2/m) c_1 \psi_2(\mathbf{R}_1)$ . The overlap integral between two wavefunctions of the form (S2.2), separated by a distance  $r$ , is given by:

$$\langle \psi_2 | \psi_1 \rangle = -\frac{2}{r} \frac{\sqrt{\alpha_1 \alpha_2}}{\alpha_1^2 - \alpha_2^2} (e^{-\alpha_1 r} - e^{-\alpha_2 r}). \quad (\text{S2.6})$$

## Overlap derivation

To estimate the overlap integral above, we position the first potential well at the origin,  $\mathbf{R}_1 = 0$ , and the second at  $\mathbf{R}_2 = r\hat{e}_z$ , where  $r$  is the separation distance between the two defects. In spherical coordinates, the wave functions are defined as follows:

$$\begin{aligned}\psi_1(\rho, \theta, \phi) &= c_1 \frac{e^{-\alpha_1 \rho}}{\rho}, \\ \psi_2(\rho, \theta, \phi) &= c_2 \frac{e^{-\alpha_2 \sqrt{\rho^2 + r^2 - 2\rho r \cos \theta}}}{\sqrt{\rho^2 + r^2 - 2\rho r \cos \theta}}.\end{aligned}$$

The overlap integral  $\langle \psi_2 | \psi_1 \rangle$  then takes the form:

$$\begin{aligned}\langle \psi_2 | \psi_1 \rangle &= c_1 c_2 \int_0^{2\pi} d\phi \int_0^\pi d\theta \sin \theta \int_0^\infty d\rho \rho^2 \frac{e^{-\alpha_1 \rho}}{\rho} \frac{e^{-\alpha_2 \sqrt{\rho^2 + r^2 - 2\rho r \cos \theta}}}{\sqrt{\rho^2 + r^2 - 2\rho r \cos \theta}} \\ &= 2\pi c_1 c_2 \int_0^\pi d\theta \sin \theta \int_0^\infty d\rho \rho \frac{e^{-\alpha_1 \rho - \alpha_2 \sqrt{\rho^2 + r^2 - 2\rho r \cos \theta}}}{\sqrt{\rho^2 + r^2 - 2\rho r \cos \theta}},\end{aligned}$$

By substituting  $u = \cos \theta$  and  $du = -\sin \theta d\theta$ , the integral simplifies to:

$$\begin{aligned}\langle \psi_2 | \psi_1 \rangle &= 2\pi c_1 c_2 \int_0^\infty d\rho \int_{-1}^1 du \rho \frac{e^{-\alpha_2 \sqrt{\rho^2 + r^2 - 2\rho r u} - \alpha_1 \rho}}{\sqrt{\rho^2 + r^2 - 2\rho r u}} \\ &= 2\pi c_1 c_2 \int_0^\infty d\rho \underbrace{\int_{-1}^1 du e^{-\alpha_1 \rho} \frac{\rho e^{-\alpha_2 \sqrt{\rho^2 + r^2 - 2\rho r u}}}{\sqrt{\rho^2 + r^2 - 2\rho r u}}}_{I_u}.\end{aligned}$$

To estimate  $I_u$ , we make a further substitution:

$$v = e^{-\alpha_2 \sqrt{r^2 - 2\rho r u + \rho^2}}, \quad \text{with } dv = \alpha_2 r \frac{\rho e^{-\alpha_2 \sqrt{r^2 - 2\rho r u + \rho^2}}}{\sqrt{r^2 - 2\rho r u + \rho^2}} du,$$

which transforms the integral to:

$$I_u = \frac{1}{\alpha_2 r} e^{-\alpha_1 \rho} \int_{v(-1)}^{v(1)} dv = \frac{1}{\alpha_2 r} \left( \underbrace{\exp[-\alpha_1 \rho - \alpha_2 \sqrt{(r - \rho)^2}]}_{I_{u_1}} - \underbrace{\exp[-\alpha_1 \rho - \alpha_2 \sqrt{(r + \rho)^2}]}_{I_{u_2}} \right).$$

We first estimate the integral  $I_1 = \int_0^\infty d\rho I_{u_1}$  by splitting it into two ranges:

$$\begin{aligned}I_1 &= \int_0^\infty d\rho \exp[-\alpha_1 \rho - \alpha_2 \sqrt{(r - \rho)^2}] \\ &= \int_0^r d\rho \exp[-(\alpha_1 - \alpha_2)\rho - \alpha_2 r] + \int_r^\infty d\rho \exp[-(\alpha_1 + \alpha_2)\rho + \alpha_2 r] \\ &= -\frac{e^{-\alpha_1 r} - e^{-\alpha_2 r}}{\alpha_1 - \alpha_2} + \frac{e^{-\alpha_1 r}}{\alpha_1 + \alpha_2}.\end{aligned}$$

The integral  $I_2 = \int_0^\infty d\rho I_{u_2}$  estimates to

$$I_2 = \int_0^\infty d\rho \exp[-\alpha_1 \rho - \alpha_2(r + \rho)] = \frac{e^{-\alpha_2 r}}{\alpha_1 + \alpha_2}.$$

The final expression for the overlap integral is estimated as follows:

$$\begin{aligned}
 \langle \psi_2 | \psi_1 \rangle &= \frac{2\pi c_1 c_2}{\alpha_2 r} \left[ -\frac{e^{-\alpha_1 r} - e^{-\alpha_2 r}}{\alpha_1 - \alpha_2} + \frac{e^{-\alpha_1 r}}{\alpha_1 + \alpha_2} - \frac{e^{-\alpha_2 r}}{\alpha_1 + \alpha_2} \right] \\
 &= -\frac{2\pi c_1 c_2}{\alpha_2 r} \frac{2\alpha_2 (e^{-\alpha_1 r} - e^{-\alpha_2 r})}{\alpha_1^2 - \alpha_2^2} \\
 &= -\frac{2}{r} \frac{\sqrt{\alpha_1 \alpha_2}}{(\alpha_1^2 - \alpha_2^2)} (e^{-\alpha_1 r} - e^{-\alpha_2 r})
 \end{aligned}$$

In the case when both wells are identical  $\alpha_2 = \alpha_1 = \alpha$  the integral simplifies to:

$$\langle \psi_2 | \psi_1 \rangle|_{\alpha=\alpha_1=\alpha_2} = e^{-r\alpha}.$$

Using the equation above, the transfer integral becomes

$$W = \langle \psi_1 | H | \psi_2 \rangle = \frac{\hbar^2}{mr} \frac{\sqrt{\alpha_1 \alpha_2}}{(\alpha_1^2 - \alpha_2^2)} (\alpha_2^2 e^{-\alpha_1 r} - \alpha_1^2 e^{-\alpha_2 r}) \quad (\text{S2.7})$$

### Derivation

$$\begin{aligned}
 \langle \psi_1 | H | \psi_2 \rangle &= -\frac{\alpha_2^2 \hbar^2}{2m} \langle \psi_1 | \psi_2 \rangle - \frac{\sqrt{\alpha_1 \alpha_2} \hbar^2}{mr} e^{-\alpha_2 r} \\
 &= \frac{\hbar^2}{mr} \left( \frac{\alpha_2^2 \sqrt{\alpha_1 \alpha_2} (e^{-\alpha_1 r} - e^{-\alpha_2 r})}{(\alpha_1^2 - \alpha_2^2)} - \sqrt{\alpha_1 \alpha_2} e^{-\alpha_2 r} \right) \\
 &= \frac{\hbar^2}{mr} \frac{\sqrt{\alpha_1 \alpha_2}}{(\alpha_1^2 - \alpha_2^2)} [\alpha_2^2 (e^{-\alpha_1 r} - e^{-\alpha_2 r}) - (\alpha_1^2 - \alpha_2^2) e^{-\alpha_2 r}] \\
 &= \frac{\hbar^2}{mr} \frac{\sqrt{\alpha_1 \alpha_2}}{(\alpha_1^2 - \alpha_2^2)} [\alpha_2^2 e^{-\alpha_1 r} - \alpha_2^2 e^{-\alpha_2 r} - \alpha_1^2 e^{-\alpha_2 r} + \alpha_2^2 e^{-\alpha_2 r}] \\
 &= \frac{\hbar^2}{mr} \frac{\sqrt{\alpha_1 \alpha_2}}{(\alpha_1^2 - \alpha_2^2)} (\alpha_2^2 e^{-\alpha_1 r} - \alpha_1^2 e^{-\alpha_2 r})
 \end{aligned}$$

### S2.B. Approximation of Zero Wavefunction Overlap

In the model described above, we introduce an additional approximation that neglects the overlap between the wavefunctions. Under this assumption, the transfer integral simplifies to:

$$\begin{aligned}
 W_A &= \frac{1}{2} \langle \psi_1 | T + V_1 + T + V_2 + V_1 + V_2 | \psi_2 \rangle \\
 &= \frac{1}{2} \langle \psi_1 | V_1 + V_2 | \psi_2 \rangle \\
 &= -\frac{\hbar^2}{2mr} \sqrt{\alpha_1 \alpha_2} (e^{-\alpha_1 r} + e^{-\alpha_2 r}). \quad (\text{S2.8})
 \end{aligned}$$

To compare the two models, we use experimental parameters for the defects. The binding energy of nitrogen is  $|E_2| = 1.7$  eV, and that of the NV center is  $|E_1| = 2.6$  eV. For benchmarking, we adopt an electron effective mass of  $m = 0.35, m_e$ . Using  $\alpha_i = \sqrt{2m|E_i|}/\hbar$ , the corresponding well parameters are:

$$\begin{aligned}
 \alpha_1 &= 0.209 a_B^{-1}, \\
 \alpha_2 &= 0.259 a_B^{-1},
 \end{aligned}$$

where  $a_B$  is the Bohr radius, corresponding to 0.529 Å.

Figure S3 compares  $W^2$  calculated using the full treatment, which includes wave function overlaps as described by Eq. (S2.7), with the zero-overlap approximation given by Eq. (S2.8). The bottom panel of the figure shows the ratio

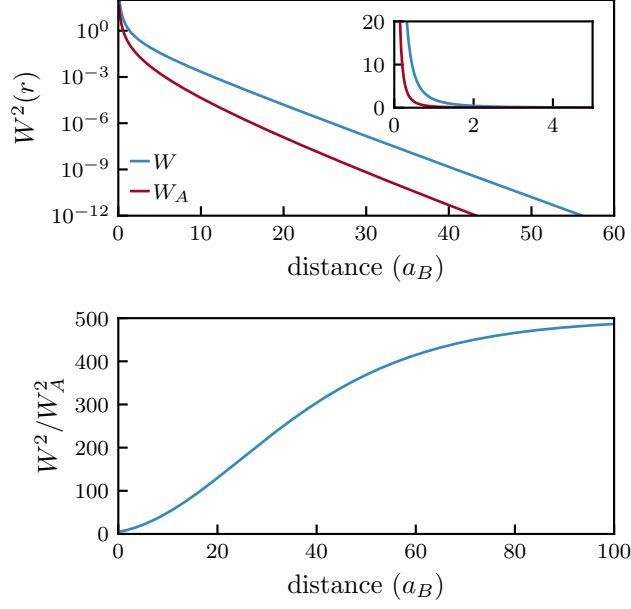


FIG. S2. Comparison of  $W^2$  calculated using the full treatment (including overlaps) and the zero-overlap approximation. The bottom panel shows the ratio of the two models.

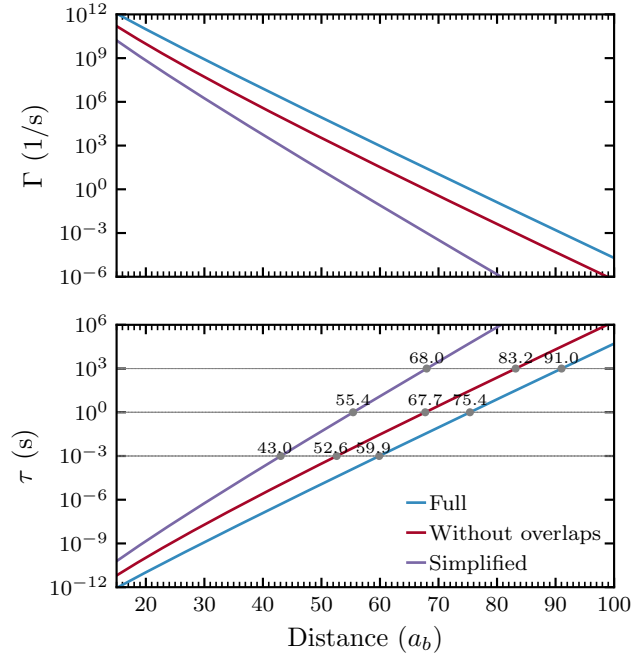


FIG. S3. Comparison of calculated rates and lifetimes using the full treatment (including overlaps) the zero-overlap approximation and single exponential.

of the two models, indicating the differences between them. We find that neglecting wave function overlaps results in a significantly faster decay of  $W^2$  with increasing distance. This demonstrates the important role of wave function overlaps in providing an accurate qualitative and quantitative description of the transfer integral.

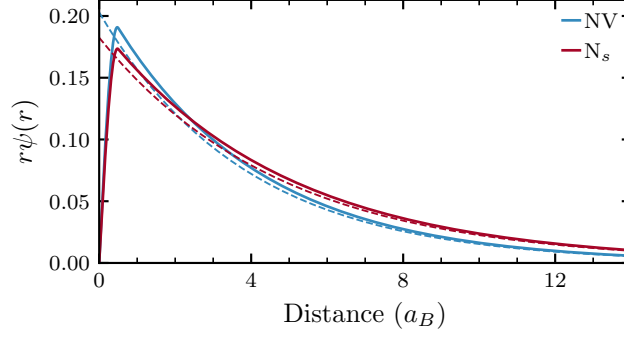


FIG. S4. Radial wavefunctions  $r\psi(r)$  for the ZRP and finite spherical well models. The dashed lines represent the ZRP wavefunctions, while the solid lines correspond to the finite spherical well model.

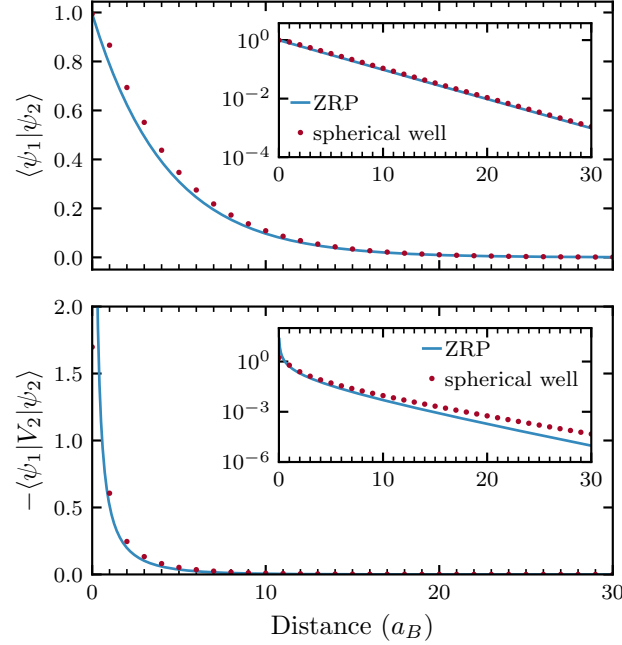


FIG. S5. Comparison of overlaps and potential term contributions  $-\langle\psi_2|V_2|\psi_1\rangle$  for the ZRP and finite spherical well models. The analytical expressions (Eqs. (S2.5c) and (S2.6)) are shown alongside the numerical results.

### S2.C. Benchmarking the Zero-Range Potential Model Against a Finite Spherical Well

While the zero-range potential (ZRP) model provides a simplified and analytically tractable framework, it neglects the finite potential depth and spatial extent, which can influence tunneling dynamics. To evaluate the accuracy of the ZRP model in describing electron tunneling between two deep defects, we benchmark it against a more realistic model involving finite spherical wells, defined by the potential:

$$V(r) = \begin{cases} -V_0 & r \leq a, \\ 0 & r > a, \end{cases}$$

where  $a$  is the radius of the potential well. In this study, we set  $a = a_B/2$ , where  $a_B$  is the Bohr radius. The depth of the potential well,  $V_0$ , is chosen to ensure that the system supports a single bound state with an ionization energy matching those of the actual NV and N defects. This yields  $V_0 = 425.44$  eV and  $V_0 = 417.203$  eV for the NV and N centers, respectively.

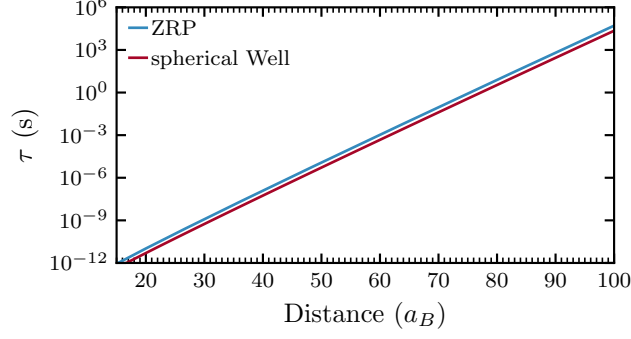


FIG. S6. Comparison of numerically calculated tunneling rates with the analytical expression of Eq. (S2.7).

In Fig. S4, we compare the radial dependence of the spherical well wavefunctions  $r\psi_i(r)$  with the corresponding ZRP wavefunctions,  $c_i \exp(-\alpha_i r)$ , shown as dashed lines. In Fig. S5, we present the numerically calculated overlaps and the potential term contributions  $-\langle\psi_2|V_2|\psi_1\rangle$ . These results are compared with the analytical expressions provided in Eqs. (S2.5c) and (S2.6), demonstrating strong agreement. Finally, in Fig. S6, we compare the numerically calculated tunneling rates with the analytical expression of Eq. (S2.7).

This analysis demonstrates that the ZRP model closely reproduces the tunneling behavior of two narrow, finite-dimensional spherical wells, validating its applicability as an effective approximation for electron transfer.

### S3. POPULATION BUILDUP DURING IONIZATION STAGE

In the experiment, the ensemble is excited by 620 nm laser pulses at a repetition rate of 10 kHz (pulse spacing  $\Delta t = 100 \mu\text{s}$ ) with an average power of approximately 100  $\mu\text{W}$ . For the timescales considered here, the sequence of optical pulses can be treated as a continuous-wave (CW) excitation characterized by an average ionization rate  $G$ . Ionization of  $\text{NV}^-$  centers during this stage produces a transient  $\text{NV}^0$  population  $P$  that can be described by a rate equation:

$$\frac{dP}{dt} = -\Gamma P + (1 - P)G, \quad (\text{S3.9})$$

where  $P$  is the instantaneous  $\text{NV}^0$  population,  $\Gamma$  is the recombination rate, and  $G$  is the effective average ionization rate. The analytical solution of Eq. (S3.9) with  $P(t_0) = 0$  is

$$P(t) = \frac{G}{\Gamma + G} \left( 1 - e^{-(\Gamma + G)(t - t_0)} \right). \quad (\text{S3.10})$$

The population immediately after pumping for a duration  $\Delta t$  is

$$P(\tau; \Delta t) = \frac{G}{\Gamma + G} \left( 1 - e^{-(\Gamma + G)\Delta t} \right) \quad (\text{S3.11})$$

Equation (S3.11) defines the filter function  $f(\tau; \Delta t)$ , which quantifies how efficiently a subensemble with lifetime  $\tau = 1/\Gamma$  builds up population during the ionization stage.

Since the ionization process proceeds via two-photon absorption, it is relatively slow, and the resulting ionization rate  $G$  can be assumed to be small. In the weak-excitation limit ( $G \ll \Gamma$ ), this simplifies to

$$f(\tau; \Delta t) \approx G\tau(1 - e^{-\Delta t/\tau}). \quad (\text{S3.12})$$

In this model, the transient  $\text{NV}^0$  population as a function of the distance between the nitrogen and NV centers immediately after the pump laser is switched off is given by

$$w_{\text{eff}}(r) = w(r) f(\tau[r]; \Delta t),$$

where  $w(r)$  is the radial probability distribution of NV-N pairs,  $\tau[r]$  is the corresponding tunneling lifetime, and  $r$  denotes the separation between the nitrogen and NV centers.



#### S4. NV IN THE ENSEMBLE OF $N_s$ DEFECTS

Let us now examine an ensemble of NV centers interacting with an ensemble of N defects. The concentration of N defects, denoted as  $n$ , is assumed to be much higher than the concentration of NV centers. Therefore, at thermodynamic equilibrium, nearly all N defects are in their neutral charge state ( $N^0$ ), while the NV centers are in their negatively charged state ( $NV^-$ ). Upon photoionization of an  $NV^-$  center, an electron is excited to the conduction band, leaving the NV center in its neutral charge state ( $NV^0$ ). Charge equilibration then proceeds via tunneling: the electron is transferred from the nearest  $N^0$  donor to the photoionized NV center. This restores the negative charge state of the NV and converts that specific donor to  $N^+$ . We assume that the positive charge formed on this nearest neighbor does not last, since the ionizing excitation constantly redistributes the local charge. Therefore, when estimating the tunneling rate, it is enough to assume that all nitrogens are in their neutral charge state and to consider the distance to the closest neutral nitrogen atom.

##### S4.A. Radial Probability of the Nearest Neighbor

To estimate the probability of finding the nearest neighbor, we employ a Poissonian model for the system. This approach is valid because the probability of finding a nitrogen atom within a small volume element is low, and the likelihood of finding two N defects in an infinitesimally small volume  $dV$  is negligible. Furthermore, the occurrence of one nitrogen atom is independent of the presence of other nitrogen atoms. In such cases, the probability of finding  $k$  nitrogen substitutionals within a volume  $V$  is given by the Poisson distribution:

$$f(k, V) = \frac{\lambda^k e^{-\lambda}}{k!},$$

where  $\lambda = nV$  represents the expected number of nitrogen atoms within the volume  $V$ , and  $n$  is the concentration of nitrogen atoms. In terms of the radial distance  $r$  from the NV center, this probability is given by:

$$f(k, r) = \left( \frac{4}{3} \pi r^3 n \right)^k \frac{e^{-\frac{4}{3} \pi r^3 n}}{k!}.$$

The probability of finding the nearest neighbor in the shell between  $r$  and  $r + dr$  is the product of two factors: (1) the probability of finding zero nitrogen atoms within a sphere of radius  $r$ , given by  $f(0, r)$ ; and (2) the radial density of nitrogen atoms at distance  $r$ , expressed as  $p(r) = 4\pi r^2 n$ . Combining these factors, the radial probability distribution for the nearest N defect around a given NV center is:

$$w(r) = 4\pi r^2 n e^{-\frac{4}{3} \pi n r^3}.$$

The function  $w(r)$  reaches its peak at a distance of  $(2\pi n)^{-1/3}$ .

In the experiment, the samples used have nitrogen concentrations of  $n = 10$  and 180 ppm. As the atomic density of carbon in diamond is  $n_C = 2.612 \times 10^{-2}$  atoms/ $a_B^3$ , these nitrogen concentrations correspond to  $n = 2.612 \times 10^{-7}$  and  $4.702 \times 10^{-7}$  atoms/ $a_B^3$ , respectively. In Fig. S7, we present the radial distribution of the nearest neighbors corresponding to the densities mentioned above. As an approximation, we take the values of the distribution peaks as the mean distance between N and NV center 44.9 and 17.1 Å for 10 and 180 ppm concentrations respectively.

#### S5. EXPERIMENTAL DETAILS

The 10 ppm sample is a CVD-grown diamond (Element Six) with a total NV concentration of 4.5 ppm, of which about 3 ppm are  $NV^-$  and 1.5 ppm are  $NV^0$  in equilibrium. The 180 ppm sample is HPHT diamond with a  $NV^-$  concentration of 0.5 ppm.

For the experimental investigation of charge equilibration, we employ a pump-probe spectroscopy setup in which a pulsed pump laser impulsively excites an ensemble of NV centers, while a continuous-wave (CW) laser probes the time-resolved transmission through the sample. The setup and excitation schemes are illustrated in Fig. S8(a). Unlike conventional pump-probe configurations, where both the pump and probe are pulsed [25, 44, 45], our approach employs a CW probe laser. In pulsed setups, the time resolution is determined by the pulse duration, but the

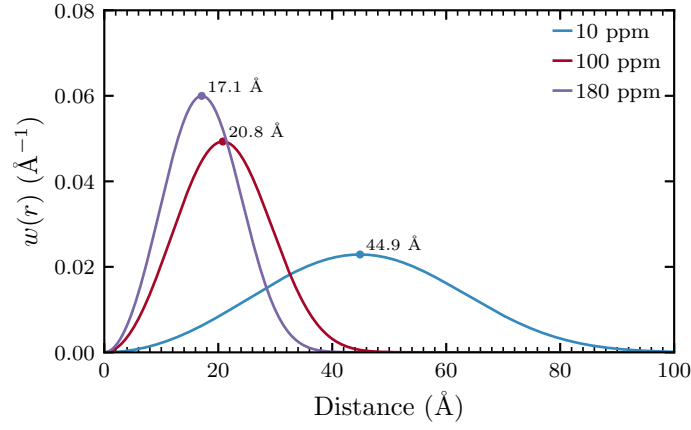


FIG. S7. Radial distribution of N defects for different concentrations. The distributions illustrate the likelihood of finding the nearest N defect at a distance  $r$  from a given NV center.

scanning range is typically limited to around 10 ns, which is insufficient for our study. By using a CW probe laser, we achieve longer time scan ranges, extending up to seconds, with the time resolution determined by the electronic bandwidth of the measurement acquisition system.

The pump pulse with a pulse duration of about 150 fs at a wavelength of 620 nm is generated in a homebuilt optical parametric amplifier (OPA) that is pumped by the output of an Ytterbium-based fiber laser (Amplitude Tangerine SP) set at a pulse repetition rate of 10 kHz. The wavelength is chosen to selectively excite  $\text{NV}^-$  but not  $\text{NV}^0$ . The CW laser, attenuated to a power of about 100  $\mu\text{W}$ , emits at a wavelength of 589 nm, which coincides with the absorption window of  $\text{NV}^-$  but not  $\text{NV}^0$ . The pump power is set to 30 mW. Both beams are collinearly combined by a polarizing beam splitter and focused to a spot size of 30  $\mu\text{m}$  on the sample, which is housed in a closed-cycle Helium cryostat. An optical bandpass filter placed after the cryostat rejects the pump light and any collected NV photoluminescence (PL), transmitting only the probe beam, which is imaged on a silicon photodiode (PD). The PD output voltage dynamics are digitized either with a fast digital oscilloscope to resolve sub-ms-long dynamics with nanosecond time resolution or with a data acquisition (DAQ) card to observe dynamics with durations beyond the millisecond range. For the latter case, the pulsed pump laser excites the sample for a duration of 200 ms, thus building up a non-equilibrium state of ionized NV centers. After switching off the pump, the system is allowed to relax back to equilibrium for up to ten seconds while monitoring this process with the probe laser. This cycle is repeated several times, and the recorded transient transmission data are averaged. In this scenario, we also employ a balanced photodetection scheme to reduce long-term probe laser fluctuations, where part of the probe beam is split off before the sample and imaged on a reference photodiode.

In order to elucidate the relaxation dynamics of photoexcited  $\text{NV}^-$  centers, we probed their ground-state bleaching (GSB) by monitoring the  $\text{NV}^-$  absorption at 589 nm. Fig. S9 shows the probe transmission transients between each pump pulse up to 100  $\mu\text{s}$  after photoexcitation (defined by the 10 kHz repetition rate), normalized to the value before excitation. The relaxation in the first 400 ns can be fitted by a bi-exponential decay model, with a fast time constant of 9 ns and a slow time constant of about 200 ns. The fast component is due to the direct relaxation to the ground state via radiative recombination, indicated by the black arrow in the inset of Fig. S9 b). The slow component is due

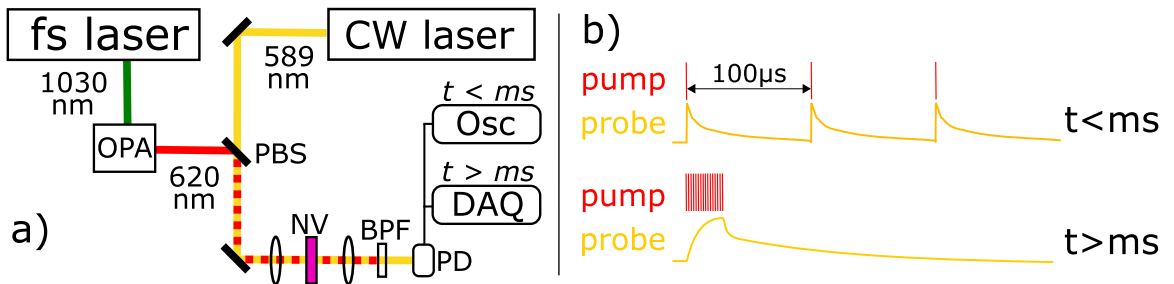


FIG. S8. a) Measurement setup, OPA: optical parametric amplifier, PBS: polarizing beam splitter, BPF: band-pass filter, PD: photodiode; b) excitation scheme for short-time (sub-ms) dynamics and long-time dynamics.

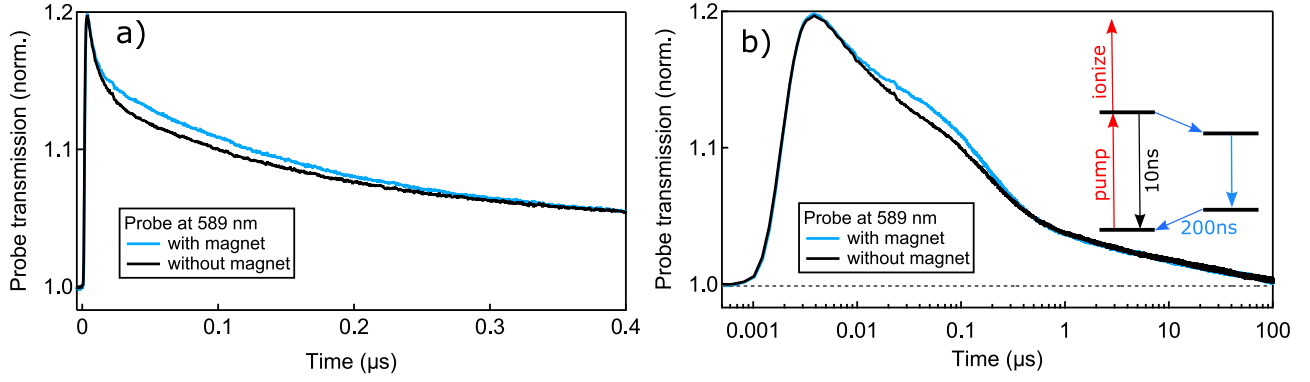


FIG. S9. Short-time transients of the probe transmission at 589 nm, with and without permanent magnet; a) up to  $0.4 \mu\text{s}$ ; b) up to  $100 \mu\text{s}$ ; the inset sketches the intrinsic  $\text{NV}^-$  electronic levels and occurring processes after photoexcitation.

to relaxation via intersystem crossing (ISC) through the singlet levels, sketched by the blue arrows [1, 25, 46]. The relaxation through the ISC path is corroborated by a modification of the transient after placing a strong permanent magnetic close to the sample (blue plot). In that case, the spin polarization in the  $\text{NV}^-$  ground state achieved through periodic excitation is scrambled, thus forcing more  $\text{NV}^-$  centers to relax via the ISC path. This effect is similar to resonant microwave driving of the  $m_s = 0$  to  $m_s = \pm 1$  transition.

If only dynamics intrinsic to  $\text{NV}^-$  were occurring, all photoexcited  $\text{NV}^-$  centers should have relaxed back to the ground state after 400 ns, with the GSB signal returning to its level before excitation, i.e. 1. This is clearly not the case because photoionized  $\text{NV}^-$  lead to the normalized probe transmission showing values  $> 1$  past  $100 \mu\text{s}$ , which is when the next pump pulse arrives. As a consequence, the train of repetitive pump pulses also slowly builds up long-time GSB bleaching past the repetition time of the laser, thus acting more like a CW laser on these longer timescales. This scenario is used for the measurements featured in the manuscript, where we probe the bleaching dynamics on millisecond to second timescales, with the pump laser output being modulated by a mechanical shutter. When opened, the long-time GSB is slowly building, as evidenced by an increase in probe transmission. After 200 ms, the pump is blocked again and the system allowed to relax without perturbation, with the bleaching dynamics being monitored by the probe laser. This cycle is repeated several times, and the recorded transient transmission data are averaged.

The data can generally be fitted well by a bi-exponential decay function, which provides a convenient way to quantitatively compare the dynamics at different temperatures. Fig. S10 shows the extracted time constants for the 10 ppm sample (a) and the 180 ppm sample (b) for a temperature range from 10K to room temperature, where no discernible temperature dependence can be recognized.

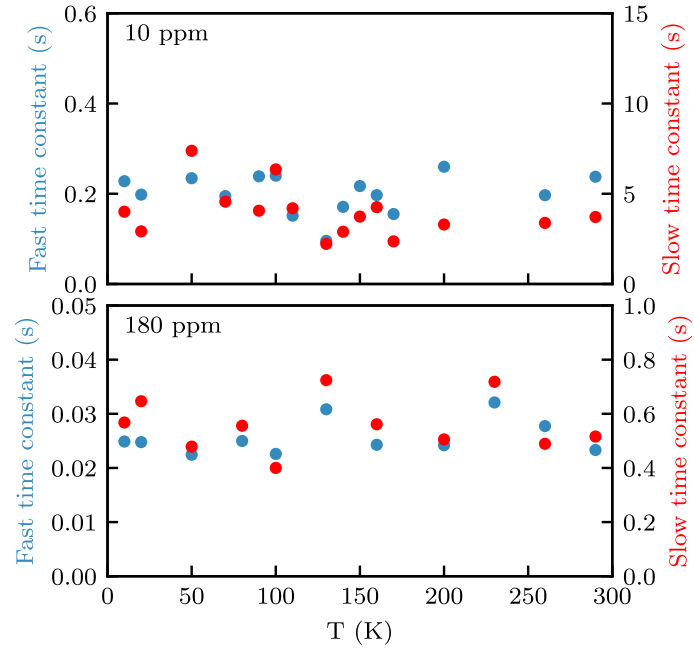


FIG. S10. Temperature dependence of the two time constants from the bi-exponential fits to the recovery dynamics of the (a) 10 ppm and (b) 180 ppm sample.